ELSEVIER

Comput. Methods Appl. Mech. Engrg. 191 (2001) 673–687

Computer methods in applied mechanics and engineering

www.elsevier.com/locate/cma

Fluid–structure interactions of a cross parachute: numerical simulation ☆

Keith Stein [a,*], Richard Benney [a], Tayfun Tezduyar [b], Jean Potvin [c]

[a] *U.S. Army Soldier and Biological Chemical Command, Soldier Systems Center, Natick, MA 01760-5017, USA*
[b] *Department of Mechanical Engineering and Materials Science, Rice University, Houston, TX, USA*
[c] *Department of Physics, Parks College, Saint Louis University, Saint Louis, MO, USA*

Received 4 August 2000; received in revised form 17 October 2000

Abstract

The dynamics of parachutes involves complex interaction between the parachute structure and the surrounding flow field. Accurate representation of parachute systems requires treatment of the problem as a fluid–structure interaction (FSI). In this paper we present the numerical simulations we performed for the purpose of comparison to a series of cross-parachute wind tunnel experiments. The FSI model consists of a 3-D fluid dynamics (FD) solver based on the Deforming-Spatial-Domain/Stabilized Space–Time (DSD/SST) procedure, a structural dynamics (SD) solver, and a method of coupling the two solvers. These FSI simulations include the prediction of the coupled FD and SD behavior, drag histories, flow fields, structural behavior, and equilibrium geometries for the structure. Comparisons between the numerical results and the wind tunnel data are conducted for three cross-parachute models and at three different wind tunnel flow speeds. © 2001 Published by Elsevier Science B.V.

Keywords: Fluid-structure interactions; Parachute simulations; Space-time formulataions; Coupled behavior

1. Introduction

In the past decade, the level of interest directed toward numerical modeling of parachute dynamics has increased dramatically, partly due to significant advances in computational methods and computer hardware. Parallel computing has seen major increases in computing power, memory, and computational methods offering solutions to problems that were until recently impossible to address. The heightened interest by the parachute community in numerical modeling, combined with advances in parallel computing technology, is making 3-D flow simulations and coupled fluid–structure computations for parachutes a real and legitimate compliment to experimental approaches (see [1–4]).

The US Department of Defense has recently focused attention towards designing a low-cost precision airdrop system for resupply and humanitarian missions. The system will be deployed at altitudes up to 25,000 ft above ground level, with up to 2200 lb. One proposed system will utilize a low-cost main cross canopy in a reefed configuration as the drogue for the majority of the system's descent. The system will transition from drogue to fully open main parachute at a prescribed altitude prior to landing.

Clearly, comparing numerical data with wind tunnel and test drop data is beneficial to both computational and experimental approaches in parachute design, because the process helps validate the computational method while improving the qualitative understanding of several sources of wind tunnel systematic errors.

☆ This paper is declared a work of the US Government and is not subject to copyright protection in the US.

0045-7825/01/$ - see front matter © 2001 Published by Elsevier Science B.V.
PII: S0045-7825(01)00312-7

As the starting point, a series of wind tunnel experiments has been performed to determine the stability, shape, flow field, surface pressure distribution, overall drag and many other parameters associated with a wide range of reefed and fully open cross-canopy configurations [5]. A subset of these wind tunnel experiments involves fully open, scaled cross parachutes with varying suspension line lengths [6]. The cross-parachute models present unique challenges due to their size and associated large wind tunnel blockage. Structural dynamic (SD) models are being developed to investigate the proposed systems such as these cross-canopy parachutes [7,8]. The main fluid dynamics (FD) model is based on the Deforming-Spatial-Domain/Stabilized Space–Time (DSD/SST) finite element formulation [9,10] of the Navier–Stokes equations of incompressible flows. The DSD/SST formulation, which was introduced earlier for flow computations involving moving boundaries and interfaces, gives us the capability to handle parachute structural deformations. Numerical simulations for the cross-parachute fluid–structure interaction (FSI) are accomplished with an FSI model we developed, which couples the SD and FD models at the parachute canopy. These methods have been tested on a variety of problems involving parachute deformations [1–3]. In this paper we present our FSI simulation strategy and the initial, first-order validations of the FSI predictions by comparing them to the wind tunnel data.

2. Governing equations

2.1. Fluid dynamics

For the FD, the air flow is assumed to be at low speeds and thus the Navier–Stokes equations of incompressible flows are utilized. Let $\Omega_t \subset \mathbb{R}^{n_{sd}}$ and $(0,T)$ be the spatial and temporal domains, respectively, where n_{sd} is the number of space dimensions, and let Γ_t denote the boundary of Ω_t. The subscript "t" implies the time-dependence of the spatial domain. The spatial and temporal coordinates are denoted by $\mathbf{x} = (x,y,z)$ and $t \in (0,T)$. The Navier–Stokes equations for incompressible flows are:

$$\rho\left(\frac{\partial \mathbf{u}}{\partial t} + \mathbf{u}\cdot\nabla\mathbf{u} + \mathbf{f}\right) - \nabla\cdot\boldsymbol{\sigma} = \mathbf{0} \quad \text{on } \Omega_t, \tag{1}$$

$$\nabla\cdot\mathbf{u} = 0 \quad \text{on } \Omega_t, \tag{2}$$

where ρ, $\mathbf{u}$, $\mathbf{f}$, and $\boldsymbol{\sigma}$ are the density, velocity, body force, and stress tensor, respectively. For a fluid with dynamic viscosity μ and the strain rate tensor $\boldsymbol{\varepsilon}(\mathbf{u})$, the stress tensor is defined as follows:

$$\boldsymbol{\sigma}(p,\mathbf{u}) = -p\mathbf{I} + 2\mu\boldsymbol{\varepsilon}(\mathbf{u}), \tag{3}$$

where $\mathbf{I}$ is the identity tensor. For the problems under consideration, μ is augmented locally using a Smagorinsky turbulence model [11]. The boundary Γ_t is composed of $(\Gamma_t)_g$ and $(\Gamma_t)_h$, corresponding to the Dirichlet- and Neumann-type boundaries, respectively. The initial condition on the velocity is specified as $\mathbf{u}(\mathbf{x},0) = \mathbf{u}_0$ on Ω_0, where $\mathbf{u}_0$ is divergence free.

2.2. Structural dynamics

Let $\Omega_t^s \subset \mathbb{R}^{n_{sd}}$ be the spatial domain bounded by Γ_t^s, where $n_{sd} = 2$ for membranes and $n_{sd} = 1$ for cables. The boundary Γ_t^s is composed of $(\Gamma_t^s)_g$ and $(\Gamma_t^s)_h$. Here, the superscript "s" corresponds to the structure. The equations of motion for the structural system are:

$$\rho^s\left(\frac{\mathrm{d}^2\mathbf{y}}{\mathrm{d}t^2} + \eta\frac{\mathrm{d}\mathbf{y}}{\mathrm{d}t} - \mathbf{f}^s\right) - \nabla\cdot\boldsymbol{\sigma}^s = 0, \tag{4}$$

where $\mathbf{y}$ is the displacement, ρ^s is the material density, $\mathbf{f}^s$ are the external body forces acting on the structure, $\boldsymbol{\sigma}^s$ is the Cauchy stress tensor, and η is the mass-proportional damping coefficient. The damping provides additional stability and has been added to problems where time-accuracy is not important.

In the finite element formulation for the SD, we use a total Lagrangian formulation of the problem. Thus, stresses are expressed in terms of the 2nd Piola–Kirchhoff stress tensor **S**, which is related to the Cauchy stress tensor through a kinematic transformation. Under the assumption of large displacements and rotations, small strains, and no material damping, the membranes and cables are treated as Hookean materials with linear-elastic properties. For membranes, under the assumption of plane stress, **S** becomes

$$S^{ij} = \left(\bar{\lambda}_m G^{ij} G^{kl} + \mu_m \left[G^{il} G^{jk} + G^{ik} G^{jl}\right]\right) E_{kl}, \tag{5}$$

where for the case of isotropic plane stress

$$\bar{\lambda}_m = \frac{2\lambda_m \mu_m}{(\lambda_m + 2\mu_m)}. \tag{6}$$

Here, E_{kl} are the components of the Cauchy–Green strain tensor, and λ_m and μ_m are the Lamé constants. For cables, under the assumption of uniaxial tension, **S** becomes

$$S^{11} = E_c G^{11} G^{11} E_{11}, \tag{7}$$

where E_c is the cable's Young's modulus. To account for stiffness-proportional material damping, the Hookean stress–strain relationships defined by Eqs. (5) and (7) are modified, and E_{kl} is replaced by $\hat{E}_{kl}$, where

$$\hat{E}_{kl} = E_{kl} + \zeta \dot{E}_{kl}. \tag{8}$$

Here, ζ is the stiffness proportional damping coefficient and $\dot{E}_{kl}$ is the time derivative of E_{kl}.

3. Finite element formulations

3.1. Fluid dynamics

To handle the time-variant spatial domains encountered in parachute problems, we employ the DSD/SST finite element formulation [9,10]. This method has been applied to a large number of problems with moving boundaries and interfaces, and is well suited to handle the canopy shape changes.

In order to construct the finite element function spaces for the space–time method, we partition the time interval $(0, T)$ into subintervals $I_n = (t_n, t_{n+1})$, where t_n and t_{n+1} belong to an ordered series of time levels $0 = t_0 < t_1 < \cdots < t_N = T$. Let $\Omega_n = \Omega_{t_n}$ and $\Gamma_n = \Gamma_{t_n}$. We define the space–time slab Q_n as the domain enclosed by the surfaces Ω_n, Ω_{n+1}, and P_n, where P_n is the surface described by the boundary Γ_t as t traverses I_n. As it is the case with Γ_t, surface P_n is decomposed into $(P_n)_g$ and $(P_n)_h$ with respect to the type of boundary condition (Dirichlet or Neumann) being imposed. For each space–time slab, we define the corresponding finite element function spaces $(\mathscr{S}^h_{\mathbf{u}})_n$, $(\mathscr{V}^h_{\mathbf{u}})_n$, $(\mathscr{S}^h_p)_n$, and $(\mathscr{V}^h_p)_n$. Over the element domain, this space is formed by using first-order polynomials in space and time. Globally, the interpolation functions are continuous in space but discontinuous in time.

The DSD/SST formulation can then be written as follows: given $(\mathbf{u}^h)_n^-$, find $\mathbf{u}^h \in (\mathscr{S}^h_{\mathbf{u}})_n$ and $p^h \in (\mathscr{S}^h_p)_n$ such that $\forall \mathbf{w}^h \in (\mathscr{V}^h_{\mathbf{u}})_n$ and $q^h \in (\mathscr{V}^h_p)_n$

$$\begin{aligned}
&\int_{Q_n} \mathbf{w}^h \cdot \rho\left(\frac{\partial \mathbf{u}^h}{\partial t} + \mathbf{u}^h \cdot \nabla \mathbf{u}^h + \mathbf{f}^h\right) \mathrm{d}Q + \int_{Q_n} \boldsymbol{\varepsilon}(\mathbf{w}^h) : \boldsymbol{\sigma}(p^h, \mathbf{u}^h)\, \mathrm{d}Q + \int_{Q_n} q^h \nabla \cdot \mathbf{u}^h \, \mathrm{d}Q \\
&\quad + \sum_{e=1}^{n_{el}} \int_{Q_n^e} \frac{\tau}{\rho}\left[\rho\left(\frac{\partial \mathbf{w}^h}{\partial t} + \mathbf{u}^h \cdot \nabla \mathbf{w}^h\right) - \nabla \cdot \boldsymbol{\sigma}(q^h, \mathbf{w}^h)\right] \cdot \left[\rho\left(\frac{\partial \mathbf{u}^h}{\partial t} + \mathbf{u}^h \cdot \nabla \mathbf{u}^h + \mathbf{f}^h\right) - \nabla \cdot \boldsymbol{\sigma}(p^h, \mathbf{u}^h)\right] \mathrm{d}Q \\
&\quad + \sum_{e=1}^{n_{el}} \int_{Q_n^e} \delta \nabla \cdot \mathbf{w}^h \rho \nabla \cdot \mathbf{u}^h \, \mathrm{d}Q + \int_{\Omega_n} (\mathbf{w}^h)_n^+ \cdot \rho\left((\mathbf{u}^h)_n^+ - (\mathbf{u}^h)_n^-\right) \mathrm{d}\Omega = \int_{(P_n)_h} \mathbf{w}^h \cdot h^h \, \mathrm{d}P.
\end{aligned} \tag{9}$$

Here, the superscript "e" refers to the element level, and τ and δ are the stabilization parameters. This process is applied sequentially to all the space–time slabs $Q_0, Q_1, Q_2, \ldots, Q_{N-1}$. The computations start with $(\mathbf{u}^h)_0^- = \mathbf{u}_0$.

In the variational formulation given by Eq. (9), the first three terms, the sixth term, and the right-hand-side constitute the Galerkin formulation of the problem. The first series of element-level integrals in Eq. (9) is least-squares terms based on the momentum equation. The second series of element-level integrals is the least-squares terms based on the incompressibility constraint, and is added to the formulation for numerical stability at high Reynolds numbers. Both stabilization terms are weighted residuals, and therefore maintain the consistency of the formulation. Since the interpolation functions are discontinuous in time, the sixth term weakly enforces continuity of the velocity field across the space–time slabs.

3.2. Structural dynamics

A semi-discrete finite element formulation for the SD equations of motion is obtained using the principle of virtual work. Finite displacements of the structure are taken into account by using a total Lagrangian description of the problem:

$$\int_{\Omega_0^s} \rho^s \frac{\mathrm{d}^2\mathbf{y}^h}{\mathrm{d}t^2} \cdot \mathbf{w}^h \,\mathrm{d}\Omega^s + \int_{\Omega_0^s} \eta\rho^s \frac{\mathrm{d}\mathbf{y}^h}{\mathrm{d}t} \cdot \mathbf{w}^h \,\mathrm{d}\Omega^s + \int_{\Omega_0^s} \mathbf{S}^h : \delta\mathbf{E}(\mathbf{w}^h) \,\mathrm{d}\Omega^s = \int_{\Omega_t^s} (\mathbf{t} + \rho^s\mathbf{f}^s) \cdot \mathbf{w}^h \,\mathrm{d}\Omega^s. \tag{10}$$

Here, the weighting function $\mathbf{w}^h$ is also the virtual displacement. The air pressure contribution is represented by vector $\mathbf{t}$. The pressure term is a "follower force" (since it "follows" the deforming structural geometry) and thus increases the overall nonlinearity of the formulation. The left-hand-side terms of Eq. (10) are referred to in the original configuration and the right-hand-side terms for the deformed configuration at time t.

Upon discretization using appropriate function spaces, a nonlinear system of equations is obtained at each time-step and can be written in the incremental form as

$$\left[\frac{\mathbf{M}}{\beta\Delta t^2} + \frac{(1-\alpha)\gamma\mathbf{C}}{\beta\Delta t} + (1-\alpha)\mathbf{K}\right]\Delta\mathbf{y}^i = \mathbf{R}^i, \tag{11}$$

where

$$\mathbf{C} = \eta\mathbf{M} + \zeta\mathbf{K}. \tag{12}$$

Here, $\mathbf{M}$ is the global mass matrix, $\mathbf{C}$ is the damping matrix, $\mathbf{K}$ is the stiffness matrix, $\mathbf{R}^i$ is the residual vector at the ith iteration, and $\Delta\mathbf{d}^i$ is the ith increment in the nodal displacement vector $\mathbf{d}$. In Eq. (11), all of the terms known from the previous iteration are lumped into the residual vector $\mathbf{R}^i$. The parameters α, β, γ are part of the Hilber–Hughes–Taylor [12] scheme which is used here to advance the solution in time.

3.3. Mesh generation and update strategy

Automatic unstructured mesh generation and automatic mesh moving schemes are used to handle the complex geometries and arbitrary deformations of the parachute canopy. These schemes introduce an increased computational cost since they involve automatic 3-D mesh generation and require the solution of an additional system of equations for the mesh motion. However, these methods are well suited for handling complex geometries and arbitrary motions for this class of problems. In this scheme, we treat the fluid mesh as a linearly elastic "pseudo-solid" that deforms as dictated by the motion of the surface boundaries of the fluid domain [13,14].

4. Problem setup

The FSI strategy consists of three components: the FD solution, the SD solution, and the coupling of the FD and SD along the fluid–structure interface. Prior to performing the FSI simulations, near equilibrium conditions for both the fluid and structure are obtained. Thus, the FSI simulation process consists of three main stages. Firstly, the SD model is generated from cut patterns of the wind tunnel parachute model and stand-alone simulations are performed using a static prescribed pressure distribution. Secondly, the resulting geometry from the SD simulation is used for computation of the unsteady flow field for that fixed parachute shape. Thirdly, the results from this flow simulation are used as the start-up condition for the FSI simulation in which the parachute is allowed to go through geometric changes.

4.1. SD model

Three cross-parachute wind tunnel models are considered. The models are each composed of a canopy section, which is constructed out of five panels (each one square foot and made of a low-porosity material), 20 suspension lines, reinforcements along the seams in the canopy (which extend from the suspension lines through the canopy), and reinforcements at the outer edges of the canopy between the suspension line attachment points. Each of the 20 suspension lines has the same length. This length is 50 in. for the first model, 45 in. for the second, and 40 in. for the third. The SD model of the canopy portion of the parachute consists of nine-noded membrane elements. The suspension lines and reinforcements are represented with two-noded cable elements. The composition of the base parachute model (with 50-inch suspension lines) is shown in Fig. 1 in a "blown-out" view. Here, the lower set of lines represents the suspension lines, the middle mesh section represents the cross canopy, and the upper set of lines represents the reinforcements in the canopy along the seams and outer edges. The inner three suspension lines for each arm of the cross parachute are constructed in a kinked configuration (as depicted in Fig. 1) so that each of the suspension lines has an identical unstretched initial length of 50 in.

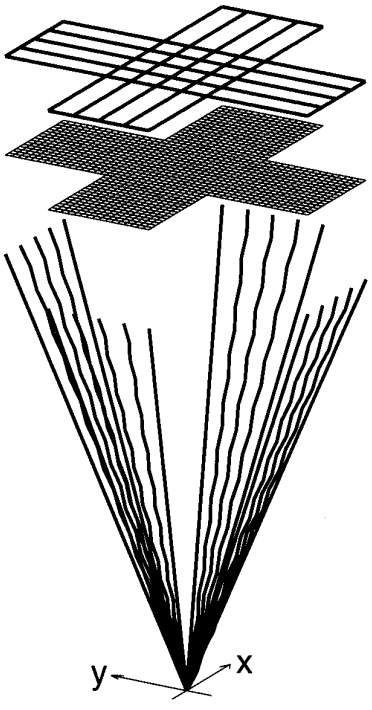

Fig. 1. Cross parachute constructed configuration.

The base wind tunnel model has a total weight of 0.50 lb. The suspension lines, canopy, and reinforcements, respectively, constitute approximately 0.23, 0.06, and 0.21 lb of the total weight. The material properties for the SD model are shown in Table 1. These values were selected to represent the wind tunnel model. Material densities were selected based on the assumed membrane thickness and cable areas to satisfy the known weight for the corresponding material groups. Linear-elastic material stiffnesses were defined to result in, for the inflated configuration, membrane and cable strains of approximately 1%. Thus, Young's moduli selected for membrane and cable materials are approximate, but representative of the cross-parachute model.

The base SD mesh consists of 5694 nodes, 1280 nine-noded membrane elements for the canopy surface, and 1488 two-noded cable elements for the suspension lines and canopy reinforcements. The suspension lines connect to a single confluence point, which represents the fixed attachment point in the wind tunnel test section. This SD mesh results in 17,079 equations.

The base model is allowed to inflate when the canopy is subjected to a prescribed nondimensional differential pressure ($\Delta p/\rho V_\infty^2$) of 1.0, where Δp is the canopy differential pressure, V_∞ is the wind tunnel velocity, and ρ is the density of air. The fully inflated equilibrium configuration for the base model is obtained with a damped, dynamic SD simulation and is shown in Fig. 2. Maximum principal stresses for the parachute canopy (membrane) are superimposed on the surface, with dark regions representing the low stresses (predominant along the canopy reinforcements) and light regions representing the high stresses. This equilibrium solution is used for defining the parachute canopy configuration in the FD model.

The SD mesh for the base model with 50-inch suspension lines is also used to define the SD models with 45-inch and 40-inch suspension lines. This is accomplished by "shrinking" the suspension lines by 5 and 10 in. in order to represent the 45-inch and 40-inch models, respectively. The shrinking is accomplished by redefining the natural lengths of the suspension line cables during dynamic stand-alone SD simulations [3,7]. The internal stresses in the cables are computed throughout the simulations based on the time-variant natural lengths. Inertial and gravitational terms are computed based on the initial lengths of the cables. Thus, the total mass of the SD models remains constant during the simulations. As the line shrinking is imposed, the 45-inch and 40-inch SD models are allowed to reach static equilibrium.

Table 1
Cross parachute: material properties

	Membranes	Cables		
Material group:	Canopy	Suspension lines	Seam reinforcements	Edge reinforcements
Thickness (area)	0.0001 ft	0.0001 ft^2	0.0001 ft^2	0.0001 ft^2
Density	3.75 slugs/ft^3	0.85 slugs/ft^3	2.0 slugs/ft^3	2.0 slugs/ft^3
Young's modulus	2×10^6 lb/ft^2	5.0×10^6 lb/ft^2	2.0×10^6 lb/ft^2	3.0×10^6 lb/ft^2
Poisson's ratio	0.3	–	–	–

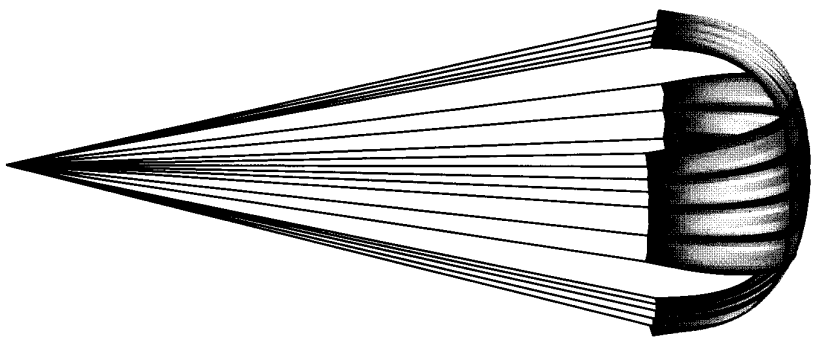

Fig. 2. Fully inflated configuration: 50-inch suspension line model.

4.2. FD model

The FD model is developed to be representative of the wind tunnel, which has a (28 in. × 39 in. × 54 in.) test section. The length of the test section is extended to the FD model to make sure that there will not be any reverse flow at the outflow boundary. The numerical model consisting of the test section and parachute canopy is shown in Fig. 3. The dashed lines represent the diverging boundaries of the wind tunnel downstream from the test section. An unstructured triangular surface mesh is generated for the fluid domain, representing the deformed canopy from the SD solution as an interior boundary. The canopy surface unstructured mesh for the inflated canopy is generated by first generating a mesh for the flat canopy, and then projecting the displacements from the SD simulation (with a structured mesh) onto the flat unstructured mesh.

This process is depicted in Fig. 4 with the flat surface mesh (upper left), the deformed SD canopy mesh with nine-noded membrane elements (upper right), and the deformed surface mesh (bottom). It should be noted that each panel in the canopy surface mesh was meshed separately in order to maintain a set of edges that define the reinforcements along the seams of the cross canopy. In addition to the outer boundaries and the canopy boundary in the FD model, an internal "refinement boundary" mesh is generated in the canopy wake region to control the level of refinement. The refinement boundary is represented by the dotted lines in Fig. 3. The complete surface mesh of the FD domain, which is sued to generate a 3-D tetrahedral volume mesh, is shown in Fig. 5 for the 50-inch SD model. For this mesh, the canopy surface is split into different, but co-located upper and lower surface nodes. This mesh generation process is performed for each of the SD models.

The initial unsteady flow solutions were obtained for the fixed-canopy configurations using a stabilized semi-discrete formulation for the FD equations [15]. This semi-discrete formulation is less cost-intensive than the DSD/SST formulation and is adequate for the stand-alone simulations since there is no time-dependence in the spatial domain (i.e., no deformations of the canopy). After the flow is developed, several time-steps were computed using the DSD/SST procedure to obtain starting FD conditions for the FSI simulations.

The boundary conditions for the FD simulations are defined to approximate the conditions of the wind tunnel: the inflow boundary is assigned a prescribed velocity condition, with constant velocity of 40, 60, or 80 miles/h; the side boundaries are assigned free-slip conditions; and the outflow boundary is assigned traction-free conditions. A zero-porosity condition is approximated for the cross-parachute canopy surface by assigning no-slip conditions. The free-slip conditions on the side boundaries used in the simulations

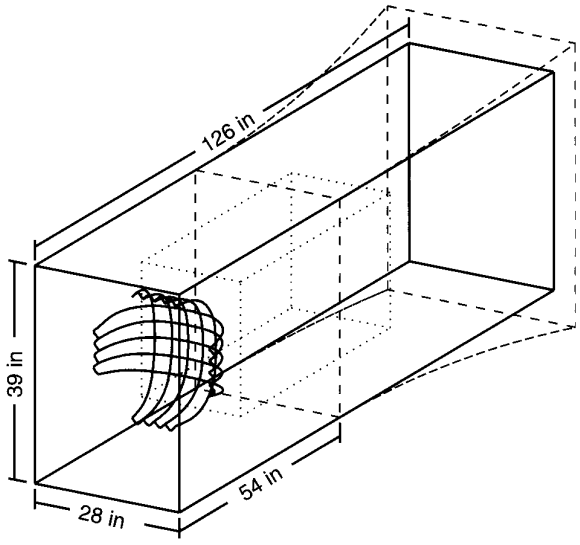

Fig. 3. Cross-parachute wind tunnel test: numerical FD domain.

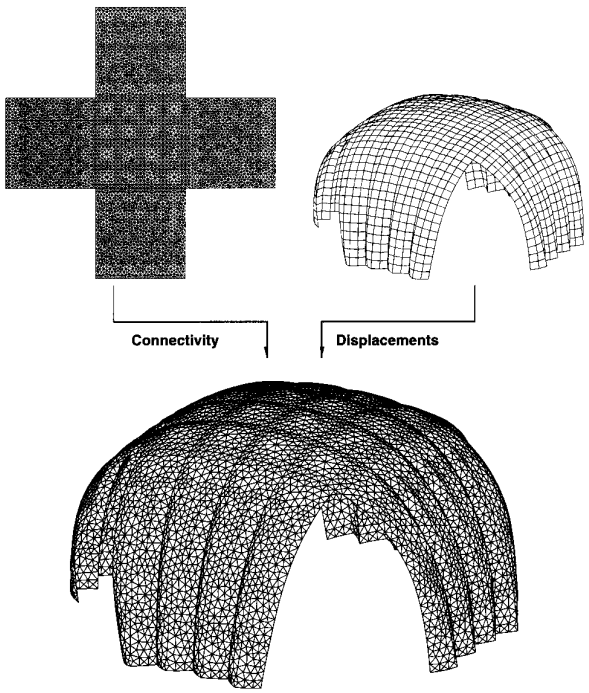

Fig. 4. Cross-parachute canopy surface mesh.

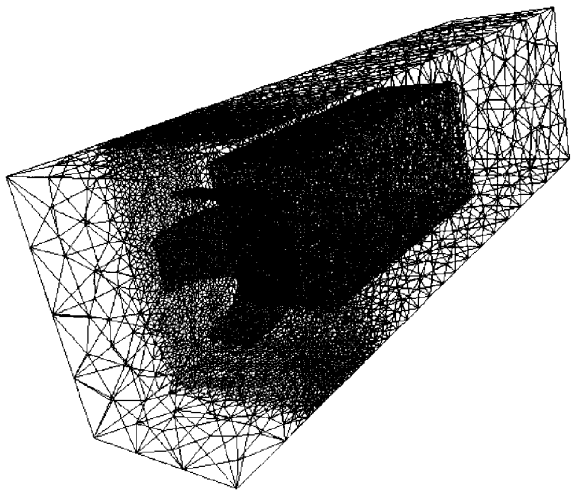

Fig. 5. Cross parachute: surface mesh of FD domain.

assume no interaction between the canopy and the wall boundary layer. Starting flow conditions are obtained for each FD mesh and for each inflow velocity.

4.3. Fluid–structure coupling

In direct coupling approaches, all fluid and structural variables are updated simultaneously by solving a single coupled system of equations. Implementation of a directly coupled solver can be overly burdensome

and for this reason we implement an "iteratively coupled" approach. Here, all variables are updated separately in a "staggered" fashion, within the nonlinear iteration loop, by solving individual systems of equations for the fluid and structure. Coupling is achieved through the transfer of FSI information between the fluid and structural solvers prior to the updates. This information is transferred along the fluid–structure interface. The displacements from the SD solution are used to update the fluid mesh. Iterative coupling approaches have been demonstrated in [1,2,16,17].

In the simulations, it is assumed that the suspension lines and the wind tunnel mounting hardware have no effect on the flow field. Simple line drag approximations are imposed as forces in the SD model. Thus, FSI coupling occurs over the cross-parachute canopy surface. The cross-canopy surface meshes for the FD and SD models are incompatible (i.e., nodally inequivalent, different element types), as depicted in Fig. 4. This approach has the benefit in that it allows for individual FD and SD meshes to be designed, with different element types, to take advantage of the strengths of each solver. However, incompatible meshes require a more complicated projection scheme for the transfer of information across the fluid–structure interface. Coupling information is transferred between the incompatible surface meshes by a least-squares projection scheme as described and demonstrated in [2,3,18]. Here, surface pressures from the FD solution are projected from the triangular FD surface mesh to the integration points of the nine-noded membrane elements in the SD mesh. Likewise, canopy displacements and displacement rates from the SD solution are projected from the SD mesh to the FD mesh. Canopy displacements from the SD computations are used as Dirichlet boundary conditions in the pseudo-solid automatic mesh moving strategy. The displacement rates from the SD computation are used to impose the no-slip boundary conditions on the canopy surface in the FD simulation.

5. Results

The time-averaged drags computed from the FSI simulations and measured from the wind tunnel experiments are summarized in Table 2 and compared in Figs. 6, 7. Fig. 6 shows, for inflow velocities of 40 and 60 miles/h, the computed and measured drags as a function of suspension line length. Fig. 7 shows, for two cross-parachute models, the computed and measured drags as a function of inflow velocity. For the plot on the right side of Fig. 7, the suspension line lengths for the FSI and wind tunnel models differ by 1 in., with the FSI model having 50-inch lines and the wind tunnel model having 51-inch lines. The plots in Figs. 6 and 7 show good agreements in the drag trends and have errors ranging from 3% to 10%.

Shape comparisons were made for the cross parachute with 50-inch suspension lines at tunnel speeds of 40 and 60 miles/h. Fig. 8 shows, for 40 miles/h, a qualitative comparison of the predicted configuration for the inflated canopy from the FSI simulation (left) and for the wind tunnel experiments (right). The projected width of the center panel of the canopy was also measured. Measurements from video data showed

Table 2
Cross-parachute drag

Simulation number	Cross-parachute model	Tunnel speed (miles/h)	Drag	
			FSI (lb)	Experiment (lb)
1	50-inch lines*	40	42.8	44.0
2	50-inch lines*	60	96.0	107.0
3	50-inch lines	80	170.5	–
4	45-inch lines	40	41.2	–
5	45-inch lines	60	92.6	–
6	45-inch lines	80	164.5	–
7	40-inch lines	40	39.6	41.0
8	40-inch lines	60	88.7	94.0
9	40-inch lines	80	157.5	–
10	28-inch lines	40	–	32.0
11	28-inch lines	40	–	62.0

*The experimental model had 51-inch lines.

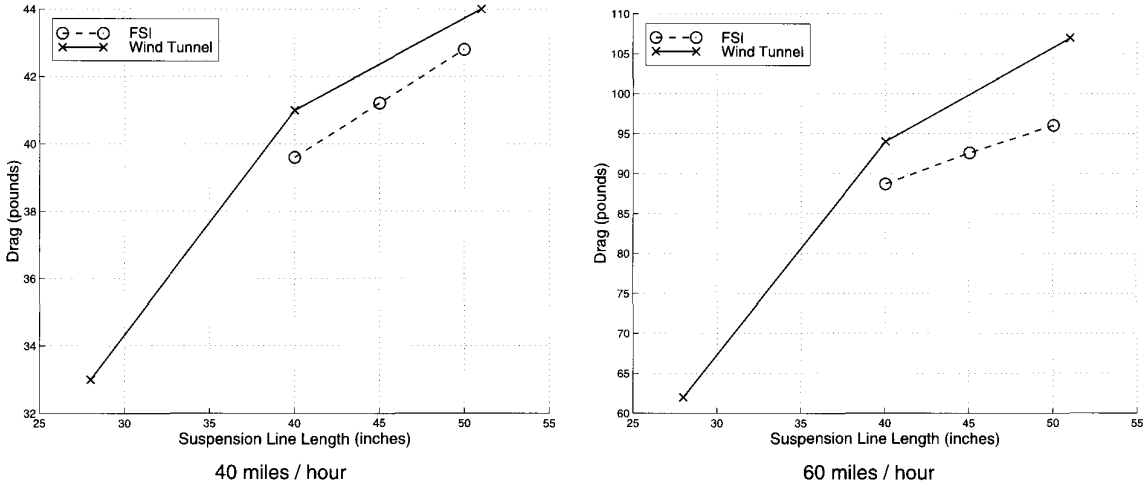

Fig. 6. Simulation and measured drags versus suspension line length.

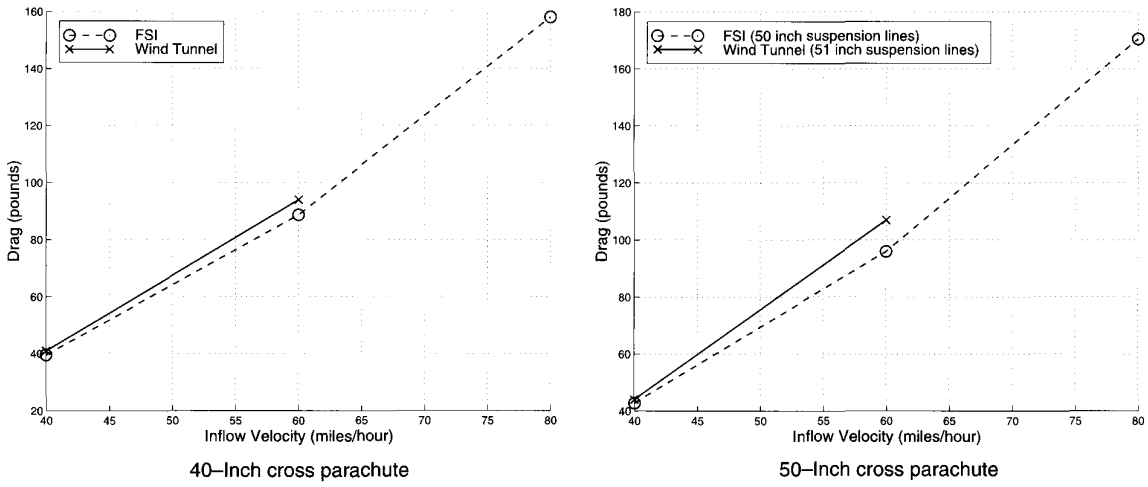

Fig. 7. Simulation and measured drags versus inflow velocity.

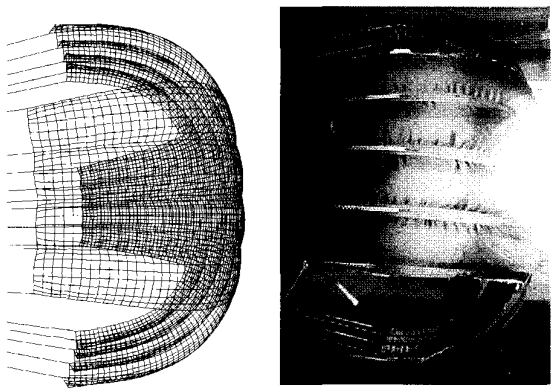

Fig. 8. Cross-parachute shape comparison.

projected widths of 11.5 ± 0.3 and 11.2 ± 0.3 in. for tunnel speeds of 40 and 60 miles/h, respectively. Average computed values for the projected widths were approximately 11.7 in. for both tunnel speeds. The deviations between the simulation and measured values are small and are most likely due to a combination of simulation approximations and measurement errors.

Several flow snapshots from the FSI simulation for the 50-inch suspension line model with an inflow of 40 miles/h are shown in Figs. 9–11. These snapshots all correspond to the same instant in time. The figures show the nondimensional pressure ($\hat{p} = (p - p_\infty)/\rho V_\infty^2$) and velocity magnitude ($V = \|u\|/V_\infty$), where p_∞ is the ambient pressure. For each of the snapshots in Figs. 9–11, the contour interval is 0.1 for pressure and 0.25 for velocity. Fig. 9 shows the $\hat{p}$- and V-contours at vertical cutting planes parallel to the inflow velocity. The four planes are positioned from the tunnel midplane (location = 14.0 in.) to the tunnel wall (location = 28.0 in.). Fig. 10 shows the $\hat{p}$- and V-contours at horizontal cutting planes parallel to the inflow velocity. The four planes are positioned from the tunnel horizontal midplane (location = 19.5 in.) to the tunnel ceiling (location = 39.0 in.). For the contours at the ceiling and side tunnel boundaries, boundary

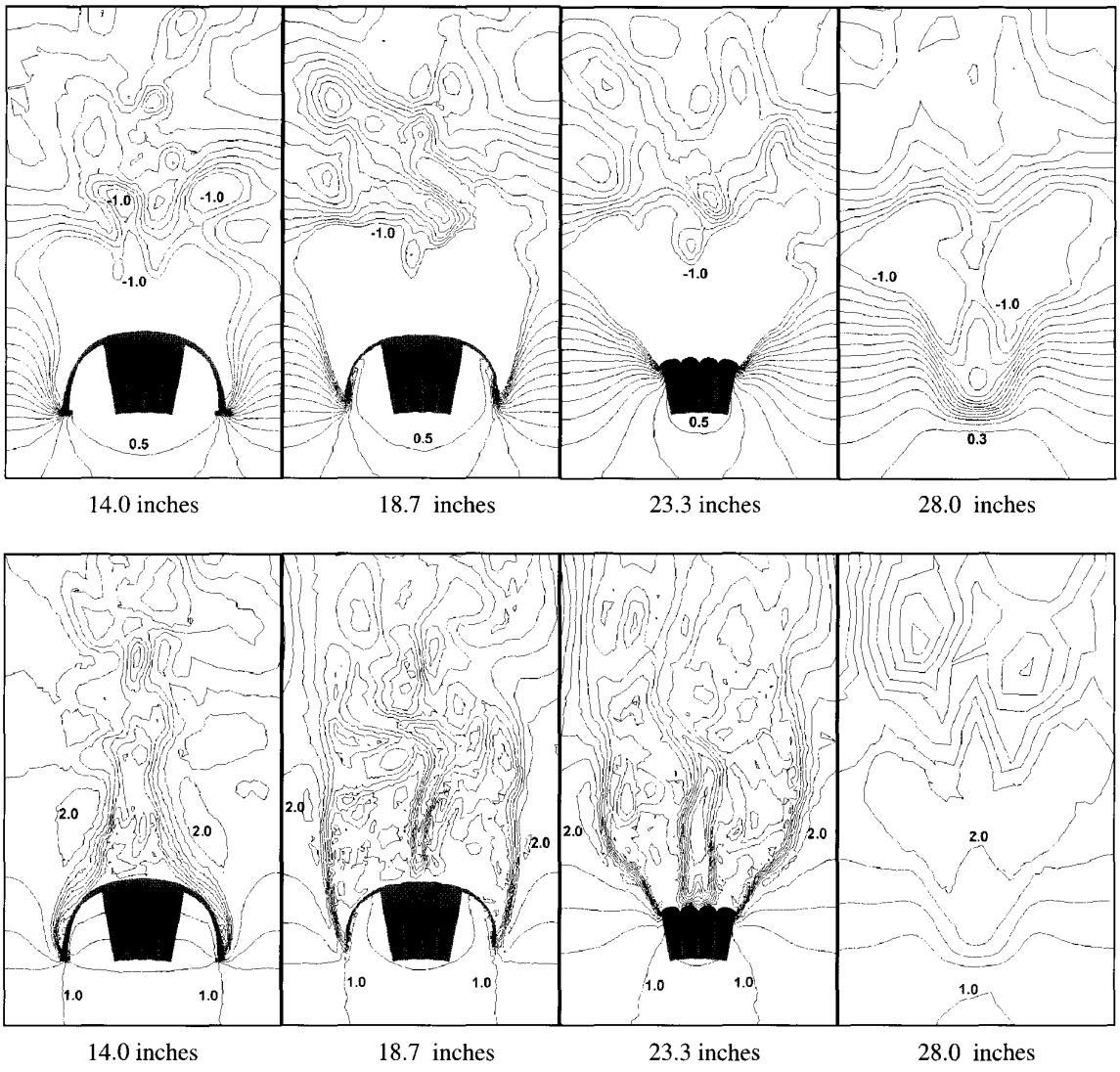

Fig. 9. Contours of pressure (top) and velocity magnitude (bottom) in vertical cutting planes.

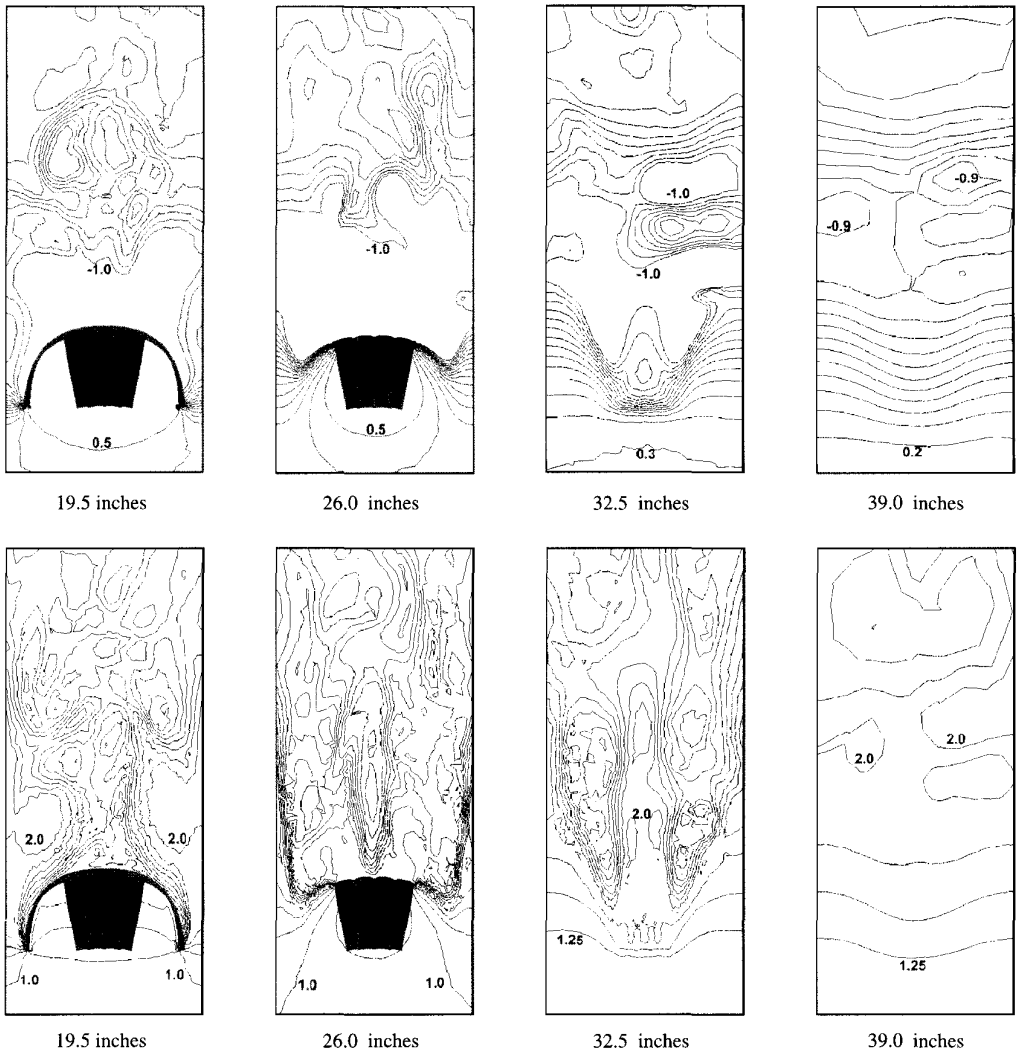

Fig. 10. Contours of pressure (top) and velocity magnitude (bottom) in horizontal cutting planes.

layer effects are neglected due to the free-slip boundary condition, and the V-contours represent the magnitude of the slip velocity along the wall. Significant blockage effects are evident due to having a rather large parachute in a small wind tunnel. As expected, blockage effects are more severe across the 28-inch width than up through the 39-inch height of the test section. This is very apparent for the flow values on the test section walls, where the blockage due to the cross canopy has a greater impact on the side walls (Fig. 9, right) than on the floor and ceiling (Fig. 10, right). Fig. 11 shows the $\hat{p}$- and V-contours at cutting planes across the tunnel and normal to the inflow velocity. The positions of the cutting planes are labelled relative to the connection points between the canopy and suspension lines. The left frame (−3.8 in.) is located upstream of the canopy. The other three cutting planes cut through the canopy surface, with the pressure contours ending at the canopy surface due to the pressure discontinuity across the surface. For the model with 50-inch suspension lines, the differential surface pressures from the FSI computations are compared with data from the wind tunnel experiments. The wind tunnel measurements yielded average differential pressures at four stations on the side of the canopy facing the ceiling of the wind tunnel test section. The four pressure ports were positioned along the center of the canopy, ranging from 1 in. from the canopy skirt to the apex (i.e., 18 in. from the skirt) (see Fig. 12). Average computed values were extracted from the

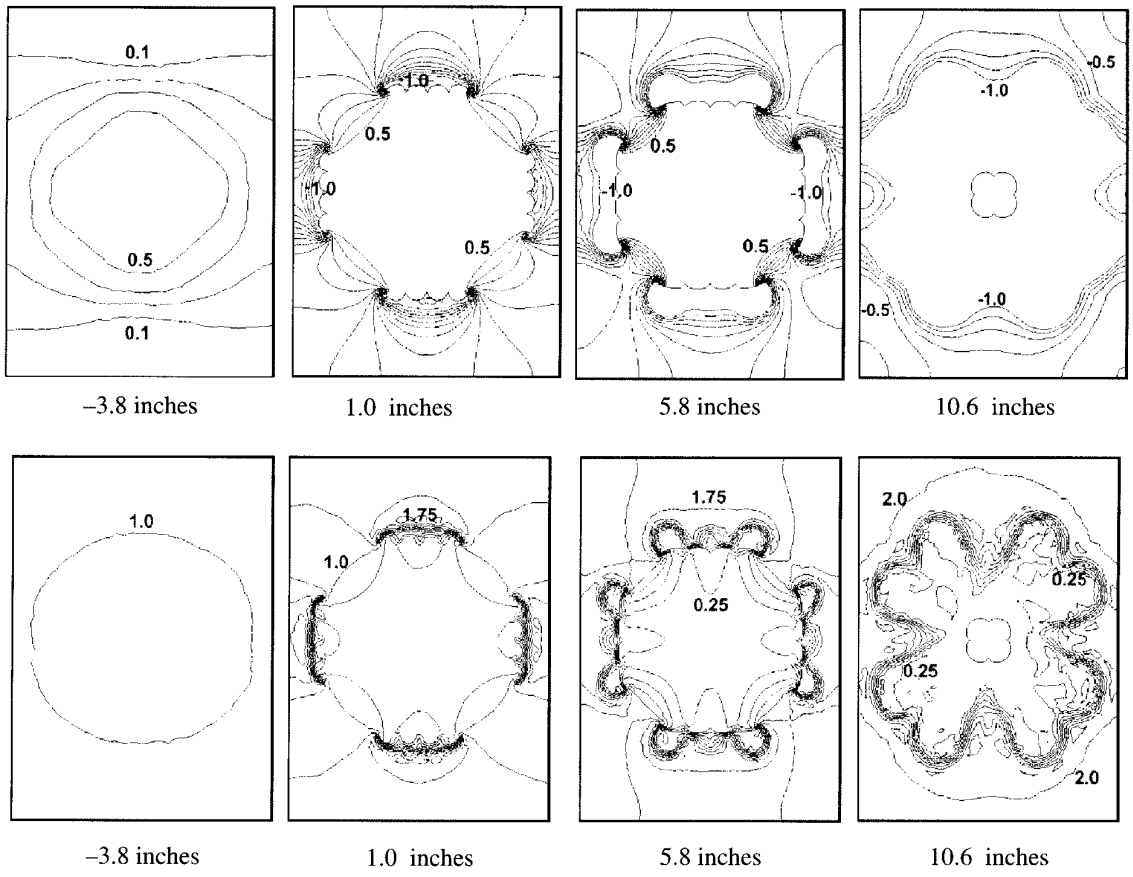

Fig. 11. Contours of pressure (top) and velocity magnitude (bottom) in cutting planes normal to the inflow velocity.

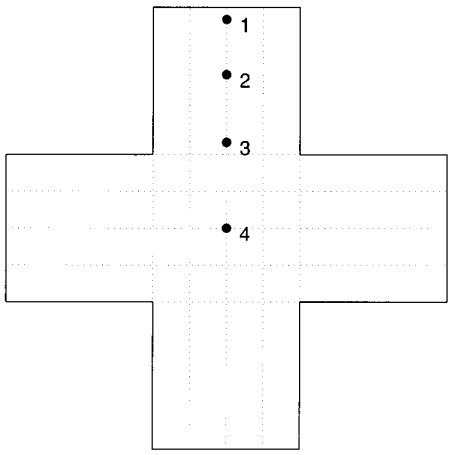

Fig. 12. Location of pressure port stations.

simulation data at corresponding locations in the FD mesh, and the comparisons between the measured and computed data are illustrated in Table 3. Here, differential pressures are shown in psi and for tunnel speeds of 40 and 60 miles/h.

Table 3
Cross parachute: differential surface pressures in psi

Station	Distance from skirt (in.)	FSI 40 miles/h	Tunnel 40 miles/h	FSI 60 miles/h	Tunnel 60 miles/h
1	1.0	0.110	0.123 ± 0.021	0.248	0.306 ± 0.021
2	5.5	0.110	0.102 ± 0.010	0.248	0.249 ± 0.010
3	11.0	0.124	0.106 ± 0.008	0.280	0.259 ± 0.008
4	18.0	0.121	0.099 ± 0.014	0.280	0.243 ± 0.014

6. Concluding remarks

Preliminary FSI simulations have been performed to numerically model a series of wind tunnel experiments with cross parachutes. The comparisons between the computed results and the wind tunnel data involve drag behavior, inflated shapes, and differential surface pressures. These preliminary simulations and comparisons establish significant confidence in our numerical model and are quite promising. The numerical model is being further refined to more precisely represent the physical test setup, and additional experiments are being conducted to further correlate comparisons between the numerical model and the physical experiments.

Acknowledgements

This work was sponsored in part by AFOSR (contract number F49620-98-1-0214), by NASA-JSC (grant number NAG9-1059), and by the Army HPC Research Center under the auspices of the Department of the Army, ARL cooperative agreement number DAAH04-9-52-0003 and contract number DAAH04-95-C-0008. The content does not necessarily reflect the position or the policy of the Government, and no official endorsement should be inferred.

References

[1] K. Stein, R. Benney, V. Kalro, T. Tezduyar, J. Leonard, M. Accorsi, Parachute fluid–structure interactions: 3-D computation, Computer Methods in Applied Mechanics and Engineering 190 (2000) 373–386.
[2] V. Kalro, T. Tezduyar, A parallel 3D computational method for fluid–structure interactions in parachute systems, Computer Methods in Applied Mechanics and Engineering 190 (2000) 321–332.
[3] K. Stein, R. Benney, V. Kalro, T. Tezduyar, J. Leonard, M. Accorsi, 3-D computation of parachute fluid–structure interactions: performance and control, in: Proceedings of the CEAS/AIAA 15th Aerodynamic Decelerator Systems Technology Conference, AIAA-99-1714, Toulouse, France, 1999.
[4] C. Ibos, C. Lacroix, A. Goy, P. Bordenave, Fluid-structure simulation of 3D Ram air parachute with Sinpa software, in: Proceedings of the CEAS/AIAA 15th Aerodynamic Decelerator Systems Technology Conference, AIAA-99-1713, Toulouse, France, 1999.
[5] J. Potvin, L. Esteve, G. Peek, R. Alamat, J. Little, Wind tunnel study of cruciform parachutes folded in various configurations, in: Proceedings of the CEAS/AIAA 15th Aerodynamic Decelerator Systems Technology Conference, AIAA-99-1739, Toulouse, France, 1999.
[6] B. Brocato, L. Esteve, D. Garcia, C. Manglano, G. Peek, J. Potvin, R. Benney, K. Stein, R. Alamat, J. Little, Experimental study of fluid–structure interactions on a cross-parachute: comparison of wind tunnel data and drop data with CFD predictions, in: Proceedings of the CEAS/AIAA 15th Aerodynamic Decelerator Systems Technology Conference, AIAA-99-1737, Toulouse, France, 1999.
[7] R.J. Benney, K.R. Stein, J.W. Leonard, M.L. Accorsi, Current 3-D structural dynamic finite element modeling capabilities, in: Proceedings of the 14th AIAA Aerodynamic Decelerator Technology Conference, AIAA-97-1506, San Francisco, 1997.
[8] R. Benney, K. Stein, W. Zhang, M. Accorsi, J. Leonard, Controllable airdrop simulations utilizing a 3-D structural dynamics model, in: Proceedings of the CEAS/AIAA 15th Aerodynamic Decelerator Systems Technology Conference, AIAA-99-1727, Toulouse, France, 1999.
[9] T.E. Tezduyar, M. Behr, J. Liou, A new strategy for finite element computations involving moving boundaries and interfaces – the deforming-spatial-domain/space–time procedure: I. The concept and the preliminary tests, Computer Methods in Applied Mechanics and Engineering 94 (1992) 339–351.

[10] T.E. Tezduyar, M. Behr, S. Mittal, J. Liou, A new strategy for finite element computations involving moving boundaries and interfaces – the deforming-spatial-domain/space–time procedure: II. Computation of free-surface flows, two-liquid flows, and flows with drifting cylinders, Computer Methods in Applied Mechanics and Engineering 94 (1992) 353–371.
[11] J. Smagorinsky, General circulation experiments with the primitive equations, Monthly Weather Review 91 (1963) 99–165.
[12] H.M. Hilber, T.J.R. Hughes, R.L. Taylor, Improved numerical dissipation for time integration algorithms in structural dynamics, Earthquake Engineering and Structural Dynamics 5 (1977) 283–292.
[13] T.E. Tezduyar, M. Behr, S. Mittal, A.A. Johnson, Computation of unsteady incompressible flows with the finite element methods – space–time formulations, iterative strategies and massively parallel implementations, in: P. Smolinski, W.K. Liu, G. Hulbert, K. Tamma (Eds.), New Methods in Transient Analysis, AMD, vol. 143, ASME, New York, 1992, pp. 7–24.
[14] A.A. Johnson, T.E. Tezduyar, Mesh update strategies in parallel finite element computations of flow problems with moving boundaries, Computer Methods in Applied Mechanics and Engineering 119 (1994) 73–94.
[15] T.E. Tezduyar, Stabilized finite element formulations for incompressible flow computations, Advances in Applied Mechanics 28 (1991) 1–44.
[16] C. Farhat, M. Lesoinne, N. Maman, Mixed explicit/implicit time integration of coupled aeroelastic problems: three-field formulation, geometric conservation, and distributed solution, International Journal for Numerical Methods in Fluids 21 (1995) 807–835.
[17] R. Löhner, C. Yang, J. Cebral, J.D. Baum, H. Luo, D. Pelessone, C. Charman, Fluid–structure interaction using a loose coupling algorithm and adaptive unstructured grids, in: Proceedings of the 36th AIAA Aerospace Sciences Meeting, Reno, 1995.
[18] N. Maman, C. Farhat, Matching fluid and structure meshes for aeroelastic computations: a parallel approach, Computers and Structures 54 (1995) 779–785.